JOURNAL OF TURBULENCE, 2018
VOL. 19, NO. 4, 297–321
https://doi.org/10.1080/14685248.2018.1424995

Taylor & Francis
Taylor & Francis Group

Geometry and scaling laws of excursion and iso-sets of enstrophy and dissipation in isotropic turbulence

José Hugo Elsas[a,b], Alexander S. Szalay[c] and Charles Meneveau[a]

[a]Department of Mechanical Engineering, Johns Hopkins University, Baltimore, MD, USA; [b]Instituto de Física, Universidade Federal do Rio de Janeiro, Rio de Janeiro, Brazil; [c]Department of Physics and Astronomy and Department of Computer Science, Johns Hopkins University, Baltimore, MD, USA

ABSTRACT

Motivated by interest in the geometry of high intensity events of turbulent flows, we examine the spatial correlation functions of sets where turbulent events are particularly intense. These sets are defined using indicator functions on excursion and iso-value sets. Their geometric scaling properties are analysed by examining possible power-law decay of their radial correlation function. We apply the analysis to enstrophy, dissipation and velocity gradient invariants Q and R and their joint spatial distributions, using data from a direct numerical simulation of isotropic turbulence at $\mathrm{Re}_\lambda \approx 430$. While no fractal scaling is found in the inertial range using box-counting in the finite Reynolds number flow considered here, power-law scaling in the inertial range is found in the radial correlation functions. Thus, a geometric characterisation in terms of these sets' correlation dimension is possible. Strong dependence on the enstrophy and dissipation threshold is found, consistent with multifractal behaviour. Nevertheless, the lack of scaling of the box-counting analysis precludes direct quantitative comparisons with earlier work based on multifractal formalism. Surprising trends, such as a lower correlation dimension for strong dissipation events compared to strong enstrophy events, are observed and interpreted in terms of spatial coherence of vortices in the flow.

ARTICLE HISTORY
Received 5 August 2017
Accepted 27 December 2017

KEYWORDS
Isotropic turbulence; chaos and fractals; direct numerical simulation

1. Introduction

Dissipation rate and enstrophy have been observables of great interest in turbulence research due to their dynamical significance for the evolution of flow and their rich spatial structure and intermittent nature [1]. In a view dating back to Kolmogorov [2,3] and Obukhov [4], the transfer of kinetic energy from large to small scales proceeds as a self-similar cascade process accompanied with increasing intermittency of intense events, and these are often associated with large values of dissipation rate and enstrophy. The presence of power-laws in the velocity spectrum, velocity structure functions and moments of velocity gradients and dissipation are seen as an indication of such self-similar behaviour.

CONTACT Charles Meneveau meneveau@jhu.edu

One of the most common ways to study the resultant intermittent behaviour has been through multifractal formalism. It has its origin in works by Kolmogorov [3] and Obukhov [4] who assumed a lognormal distribution for the dissipation rate, with alternative models proposed by Novikov and Stewart [5], Novikov [6–8], Mandelbrot [9] and Frisch et al. [10]. The multifractal approach was formalised explicitly in Frisch and Parisi [11], see also Benzi et al. [12], making connections to fractal geometry.

In such methodology, special attention is paid to the power-law scaling of high-order moments of velocity increments (structure functions) or dissipation rates. The approach then invokes a continuous distribution of fractal dimensions $D(h)$ of spatial sets where the velocity increments across a distance r scale with a local Holder exponent h, according to $|u(x+r) - u(x)| \sim r^h$ [12] ($u(x)$ is a component of the fluid velocity and r is a displacement in the same direction). A description in terms of local scaling for the dissipation rate ϵ and the distribution of its local exponents α with a fractal dimension $f(\alpha)$ has also been used [13,14]. The multifractal formalism as applied to turbulence has been reviewed in Refs. [1,11,15]. In this formalism, the directly measured quantities are the various statistical moments such as $\langle |u(x+r) - u(x)|^p \rangle$ or $\langle \epsilon_r^q \rangle$ (where ϵ_r is the dissipation averaged in a box of size r) while the fractal dimension functions $D(h)$ and $f(\alpha)$ are determined indirectly using the Legendre transformation [1] applied to the scaling exponents of the moments. The majority of these prior data analyses were done using one-dimensional (1D) experimental surrogates for dissipation rates while only in the last decade have full three-dimensional (3D) Direct Numerical Simulations (DNS) begun to approach high-enough Reynolds numbers for the possible power-law scaling to be discernible [16,17].

Inspite of the significant success of the multifractal formalism to encapsulate many different phenomena observed since (e.g. multi-point correlations [18], time correlations [19], extended self-similarity [20] and varying viscous scales [21]), direct determination of the fractal dimensions as a geometric characterisation of the sets of high-intensity events has been far less common. An early attempt to study the scale-invariance of histograms of singularities [22] and to deduce the dimension from these scalings has met with mixed success due to strong finite-size corrections and was thus limited to data at very high Reynolds numbers.

Thus, the status of power-law scaling of geometric features of strong events in turbulence remains unsettled. In the present work, we seek a geometric characterisation of high-intensity events in turbulence that does not rely on statistical moments of the variable but that identifies the high-intensity regions directly based on thresholding of the respective variables of interest. A previous study along these lines was presented by Moisy and Jimenez [23]. They applied a box-counting analysis to high-intensity enstrophy and dissipation region but did not observe power-law scaling. However, they did observe the hierarchical clustering of structures raising the possibility of power-law scaling in other quantities besides box-counting. In the present work, we ask whether power-law scaling can be identified for such geometric sets using analyses beyond box-counting, at Reynolds numbers attainable with DNS. In seeking such direct geometric observables and their possible power-law scaling, we are also motivated by other fields. For instance, the scaling analysis of geometrical properties of excursion sets has been applied for random sets in probability theory and the theory of random fields [24], and also has been used for the analysis of matter distributions in cosmology [25–27].

In this study, we employ a direct way to study regions of varying intensity of enstrophy and dissipation rate: instead of computing moments of the observable (or box-averaged observable) itself, we first define a geometric set as the set of points where the variables exceed a threshold (or fall into a range of values). We use the indicator function that takes on a value of one inside the set of interest and zero outside. Such geometric sets form convoluted clusters of complicated shapes. For example, high-intensity regions of vorticity are known to be arranged into elongated (worm-like) structures, representing vortices [28,29]. Nominally, each one of these structures would be characterised by a dimension equal to unity. However, it is also well known that these vortices are clustered into regions with possible multi-scaling properties and the scaling of a collection of such vortices is not necessarily obvious. Conversely, high-dissipation events are often thought to be distributed along sheets, although again these may have complex spatial structure not necessarily leading to a dimension of two. Once the set is identified, we then compute its two-point correlation function and seek to identify possible inertial-range power-law decay of the tails of the correlation functions. To compare our results with those of Moisy and Jimenez [23], we also perform a direct box-counting analysis of these sets to establish whether direct fractal scaling can be identified in the inertial range of turbulence.

Furthermore, we extend the analysis to the geometry of sets where both dissipation and enstrophy take on certain values. A 'joint multifractal' formalism was introduced previously [30], but was also based on scaling of joint moments rather than directly based on possible fractal scaling of the geometric objects that arise from joint distributions of enstrophy and dissipation. Besides enstrophy and dissipation, we also explore the spatial structure of sets formed by two velocity gradient invariants Q and R, observables that have elicited considerable interest in recent years [31]. The data-set to be considered for this analysis is isotropic turbulence at a Taylor-scale Reynolds number of $\mathrm{Re}_\lambda \approx 433$ obtained from DNS of forced Navier–Stokes equations [32]. We first define the variables of interest and then apply the analysis to the various quantities and joint distributions. The present analysis will be limited to isotropic turbulence at a single Reynolds number. Analysis of the effects of Reynolds number, numerical resolution and similar issues will be left for future studies.

2. Definitions and data-set

The typical observables we are interested in are scalar quantities derived from the velocity gradient tensor $\nabla\mathbf{u}$. These scalar fields describe the rate of rotation (based on the antisymmetric part of $\nabla\mathbf{u}$) and the rate of fluid material deformation (via the symmetric part of $\nabla\mathbf{u}$). Specifically, the two scalar fields that will be considered are defined according to

$$\frac{1}{2}\omega^2(\mathbf{x}) = \frac{1}{2}(\nabla\times\mathbf{u})^2 = \frac{1}{2}\epsilon_{ijk}\epsilon_{klm}\partial_i u_j \partial_l u_m \tag{1}$$

$$S^2(\mathbf{x}) = S_{ij}S_{ij}, \quad \text{where} \tag{2}$$

$$S_{ij} = \frac{1}{2}(\nabla\mathbf{u} + \nabla\mathbf{u}^T)_{ij} = \frac{1}{2}(\partial_i u_j + \partial_j u_i) \tag{3}$$

Note that the dissipation is given by $\epsilon(\mathbf{x}) = 2\nu S^2(\mathbf{x})$, where ν is the fluid kinematic viscosity. Hence, we refer to S^2 as the dissipation henceforth. A significant number of prior

studies have focused on dissipation and enstrophy such as [33–36]; also, other observables of interest are two scalar invariants of the velocity gradient tensor, called Q and R, defined by the following equations:

$$Q(\mathbf{x}) = -\frac{1}{2}\,\mathrm{Tr}[(\nabla \mathbf{u})^2] = \frac{1}{2}\omega^2 - S^2 \tag{4}$$

$$R(\mathbf{x}) = -\frac{1}{3}\,\mathrm{Tr}[(\nabla \mathbf{u})^3] = -\det \nabla \mathbf{u} \tag{5}$$

In the flow, the above observables assume a range of values, with S^2, $\omega^2/2$ being non-negative while Q, R can be both positive or negative. Excursion sets are the set of points $\mathbf{x}$ where such observables are above (or below) a certain threshold, for example $\omega^2/2 > \chi$ (χ will denote the threshold). We analyse the indicator function $\Theta_\chi(\mathbf{x})$ of the set of points which satisfies the stated condition. Given a set of interest associated with a threshold χ, we define its indicator function according to

$$\Theta_\chi(\mathbf{x}) = \begin{cases} 1, & \text{if } \mathbf{x} \in \text{ set of interest associated with threshold } \chi \\ 0, & \text{otherwise} \end{cases} \tag{6}$$

An analogous definition can be made for 'interval-based' sets, for example, we can define the region where enstrophy assumes values between χ_- and χ_+, i.e. $\chi_- < \omega^2/2 < \chi_+$. From here on, the latter regions will also be referred to as 'iso-sets', when χ_- and χ_+ are very close in value, in which the difference is much smaller then their absolute value.

Various statistical features of these sets can be used to characterise their spatial distribution. We are especially interested in the two-point structure of these sets and thus focus on the correlation function of $\Theta_\chi(\mathbf{x})$ defined as

$$\mathcal{C}_\chi(\mathbf{r}) = \langle \Theta_\chi(\mathbf{x})\Theta_\chi(\mathbf{x}+\mathbf{r})\rangle \tag{7}$$

where the average is understood as a spatial average over positions $\mathbf{x}$ when applied to statistically homogeneous flows. Note that we are not subtracting the averages of the indicator function (i.e. we do not define fluctuations of the indicator function but leave it as 0's and 1's).

In isotropic turbulence, the more compact quantity is the angular average of the 3D correlation function:

$$C_\chi(r) = \frac{1}{\mathcal{C}_\chi(\mathbf{0})}\int_{S_2} \mathcal{C}_\chi(\mathbf{r})\tilde{}\, d\Omega_{\mathbf{r}} \tag{8}$$

i.e. the normalised, radial correlation function. Phenomenologically, one may expect power-law decaying behaviour $C_\chi(r) \sim K_\chi r^{-\gamma_\chi}$ for r in the inertial range due to the expected self-similar behaviour of turbulence in that range of scales. The power-law exponent γ_χ is expected, however, to depend on the threshold. Writing the expected scaling behaviour with its dimensional dependencies and possibly a Reynolds number and

quantity-dependent prefactor K_χ, we write:

$$C_\chi(r) \sim K_\chi(\mathrm{Re}_\lambda)\left(\frac{r}{\eta}\right)^{-\gamma_\chi} ; \quad r >> \eta, \quad r < L \tag{9}$$

where η is the Kolmogorov scale and L is the integral scale of the flow. The scaling exponent γ_χ is expected to be positive, consistent with a decay of the correlation at increasing distance. A more geometric interpretation of the exponent γ_χ can be invoked by recalling that the correlation dimension D is defined based on the scaling of the correlation function according to $C_\chi(r) \sim r^{D-E}$ [37], where E is the dimensionality of the embedding space (here, $E = 3$). Thus, the dimension corresponding to a correlation decay exponent γ_χ is $D(\chi) = 3 - \gamma_\chi$.

For this work, we chose to perform our analysis on a snapshot from the Johns Hopkins Turbulence Database. The data comes from a DNS of forced isotropic turbulence performance on a 1024^3 periodic grid, using a pseudo-spectral parallel code. The attained Taylor-scale-based Reynolds number is $\mathrm{Re}_\lambda \approx 433$ time averaged over the database time period, and $\mathrm{Re}_\lambda \approx 426$ for the specific time-step used in the present analysis ($t = 0.0$). The domain is a periodic cube of size $[0, 2\pi]^3$, in which the data frames were stored after the simulation reached a statistically stationary state. Additional details of the data-set can be found in [32,38]. In order to establish the scaling range corresponding to the turbulence inertial range for comparison with the present results, we evaluate the longitudinal structure function as an average over the three Cartesian directions:

$$D_{\mathrm{LL}}(r) = \frac{1}{u_{\mathrm{rms}}^2}\frac{1}{3}\sum_{i=0}^{3}\langle(u_i(\mathbf{x} + r\mathbf{e}_i) - u_i(\mathbf{x}))^2\rangle \tag{10}$$

where $\mathbf{e}_i$ is the unit vector in the direction of the velocity component u_i, and $u_{\mathrm{rms}}^2 = \frac{1}{3}\sum_{i=0}^{3} u_i^2$ is the square of the root-mean-square (RMS) velocity.

In order to evaluate enstrophy and dissipation, the velocity gradients are calculated with spectral accuracy using Fast Fourier Transform (FFT). For our present analysis, we did not use the databases' finite differencing or Spline differencing tools since these are less accurate compared to spectral methods that were also used during the DNS. As further explained in Appendix 1, the analysis was done on a server near the database using notebooks provided by a dedicated compute environment (the SciServer system). For differentiation, a 3D FFT operation is applied to the velocity field to obtain the velocity field in Fourier space, then the components are multiplied by the respective wavenumbers (ik_j) to obtain the velocity gradient in the x_j direction. Finally, the inverse FFT is applied to obtain the velocity gradients in physical space. This allows us to obtain $A_{ij} = \partial_j u_i$ data from the velocity field $\mathbf{u}$. The observables we are interested in (dissipation S^2, enstrophy $\omega^2/2$, Q and R) are then computed in physical space.

To compute the correlation functions efficiently in 3D, a 3D FFT is applied to $\Theta_\chi(\mathbf{x})$ over the 1024^3 data-cube, yielding $\tilde{\Theta}_\chi(\mathbf{k})$ in Fourier space. To $\tilde{\Theta}_\chi\tilde{\Theta}_\chi^*$ is then applied the inverse Fourier transform, resulting in $\mathcal{C}(\mathbf{r})$, which is the full 3D two-point correlation function. The radial integration is done by evaluating a histogram based on the radial $\sqrt{|\mathbf{r}|^2}$ values computed over the resulting grid. This effectively performs the angular average by

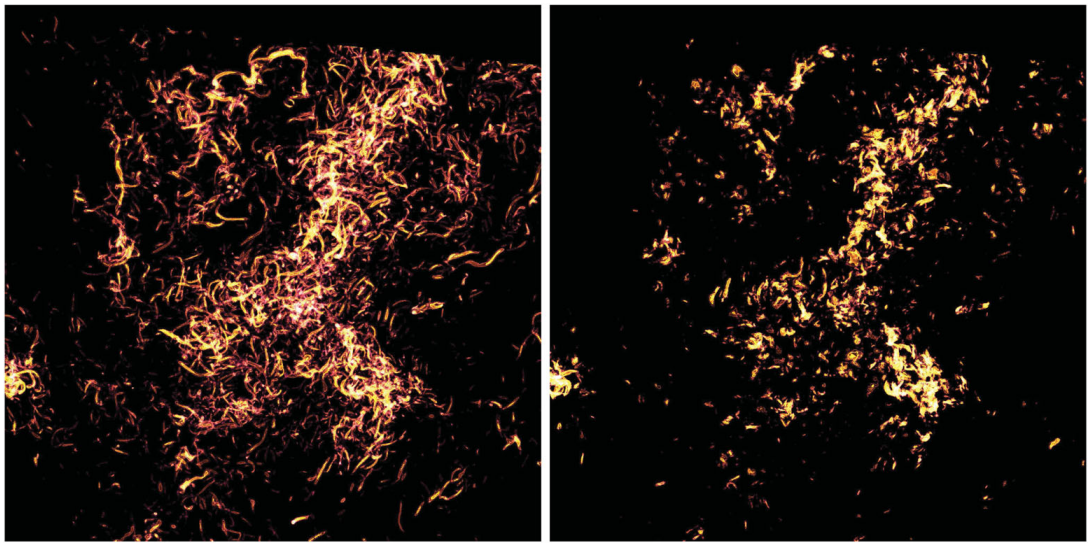

Figure 1. Volume rendering of (a) the enstrophy excursion set corresponding to the function $\frac{1}{2}\omega^2_{\text{ex}}(\mathbf{x}) = \frac{1}{2}\omega^2(\mathbf{x})\Theta^{\omega}_{20\langle S^2\rangle}(\mathbf{x})$ and (b) of the dissipation excursion set corresponding to the function $S^2_{\text{ex}}(\mathbf{x}) = S^2(\mathbf{x})\Theta^{S}_{20\langle S^2\rangle}(\mathbf{x})$ on a 512^3 subset of the full data-set, with one-eighth in volume. The visualisations were generated using the YT-project python visualisation library [39].

dividing the weighted average of the two-point correlation and the base $\sqrt{|\mathbf{r}|^2}$ histogram. More details are provided in Appendix 1.

3. Excursion set analysis

The excursion set indicator function for a given scalar field A, like enstrophy $A = \omega^2/2$ or dissipation $A = S^2$, is defined as

$$\Theta^{A}_{\chi}(\mathbf{x}) = H(A(\mathbf{x}) - \chi) = \begin{cases} 1, & \text{if } A(\mathbf{x}) \geq \chi \\ 0, & \text{otherwise} \end{cases} \tag{11}$$

where χ is the threshold applied on the scalar A. We begin by considering enstrophy excursion sets. Figure 1 shows a volume rendering of the scalar function corresponding to enstrophy above the threshold $\chi = 20\langle S^2\rangle$, given by $\frac{1}{2}\omega^2_{\text{ex}}(\mathbf{x}) = \frac{1}{2}\omega^2(\mathbf{x})\Theta_{20\langle S^2\rangle}(\mathbf{x})$. Note for consistency, all threshold values are indicated as multiples of $\langle S^2\rangle$ which are equally relevant to enstrophy here since in isotropic turbulence $\langle S^2\rangle = \frac{1}{2}\langle\omega^2\rangle$. As can be seen in Figure 1(a), this set has a very rich structure with familiar elongated strong vortices visible.

As a comparison, we also present in Figure 1(b) the visualisation of the dissipation field for the same threshold, i.e. $S^2_{\text{ex}}(\mathbf{x}) = S^2(\mathbf{x})\Theta^{S}_{20\langle S^2\rangle}(\mathbf{x})$, which provides us with some useful insights. The most striking feature is that the overall geometric distribution of high-intensity regions for dissipation closely follows the ones for high enstrophy, though the smaller scale details differ. The second feature is that at small-scales, the dissipation appears to be less 1D-like and more sheet-like, but that when viewed at larger scales, in comparison to its enstrophy counterpart. As will be seen, this fact will be visible also quantitatively in the correlation function results.

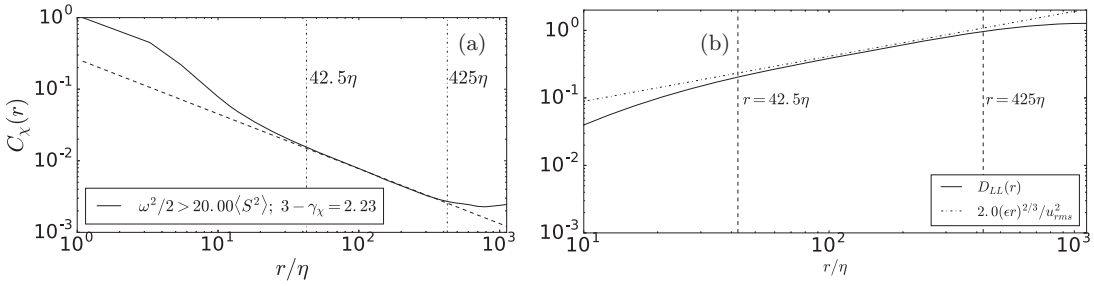

Figure 2. (a) Radial two-point correlation function for the $\omega^2/2 > 20\langle S^2\rangle$ excursion set. (b) Second-order longitudinal velocity structure function D_{LL} as function of distance r. The dotted line is the classical Kolmogorov prediction for the longitudinal second-order structure function with $C_1 = 2.0$ (the small difference with the leading coefficient that is usually closer to $C_1 \approx 2.1$ can be attributed to statistical convergence since we are only using a single snapshot).

3.1. Correlation function-based scaling

The radial two-point correlation function of the enstrophy excursion set corresponding to $\chi = 20\langle S^2\rangle$ is plotted in log–log axes in Figure 2(a). A power-law tail is clearly visible over about a decade, between $42.5\ \eta < r < 425\ \eta$. This range corresponds, roughly, to the inertial range of the studied data-set. For direct comparison, we computed the second-order structure functions for the data-set, as shown in Figure 2(b). The structure function has a scaling exponent of about $\xi_2 = 0.68$ which is the known value (slightly above the K41 value of 2/3 due to intermittency, [1]). These plots allow us to compare the quality and range of the power-laws found in both observables. The most important fact to notice is that the range where the two-point correlation function exhibits a near power-law behaviour (the interval $42.5\ \eta < r < 425\ \eta$) is the same as in the structure function. A similar behaviour will be observed for all the excursion, iso-sets and joint distribution sets studied in this work.

The scaling exponent observed in Figure 2 for the enstrophy excursion set at the given threshold is about $\gamma_\chi \approx 0.76$, implying a 'correlation dimension' of about $D(\chi) \approx 2.23$. Thus, while the topology of each individual vortex structure is visibly more 1D, as a set its two-point structure is significantly more 'space-filling' with a correlation structure that decays more slowly on average than a collection of isolated vortices.

It is important to note that correlation functions were evaluated for the indicator function distribution directly (i.e. a field of ones and zeros), and not the 'fluctuation' of the indicator function away from its spatial mean which would include negative values by necessity. We also tried to perform calculations on the subtracted version of the correlation function, but the resulting correlation functions do not present as clear a power-law behaviour in the inertial range as the one without subtracting the mean. One plausibility argument for this observation is that the correlation function without subtracting the mean more readily corresponds to the definition of the mass dimension in which the mass in spheres of radius r is evaluated, and scaling with distance r is used to define the mass dimension [37].

3.2. Box-counting-based dimensions

As an independent measure of fractal dimension for the excursion sets, we can also compute the box-counting dimension and the box-counting-based correlation dimension. The

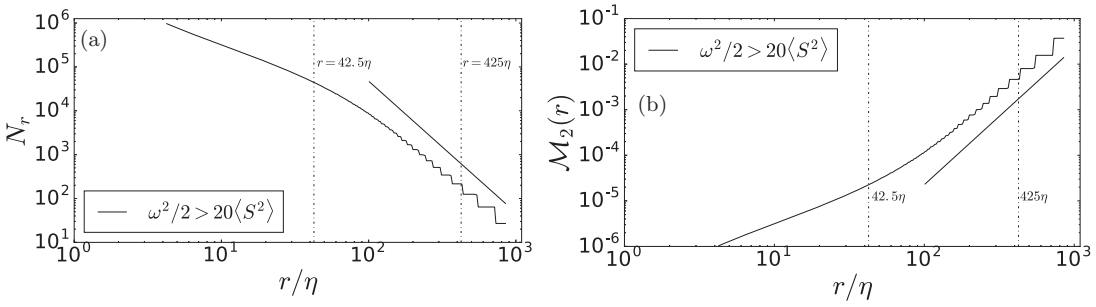

Figure 3. (a) Box-counting dimension plot for the enstrophy excursion set with threshold $\chi = 20\langle S^2 \rangle$. (b) Box-counting-based correlation dimension plot for the same set. The black line represents the $D_0 = D_2 \sim 3$ scaling expected for large scales of the box-counting calculation, since at large scales the clusters appear space-filling.

box-counting procedure for evaluating both of these dimensions is based on a set of cubes $B_{r,\mathbf{k}}$ of size r and location identified by indices $\mathbf{k} = (k_1, k_2, k_3)$ so that a cube's corner is located at $[k_1 r, k_2 r, k_3 r]$ with $k_1, k_2, k_3 \in \mathbb{Z}$, and $0 \leq k_i \leq \lceil 2\pi/r \rceil$. We assign a measure to each cube, given by

$$\mu_\chi(B_{r,\mathbf{k}}) = \frac{1}{V_{2\pi}} \int_{B_{r,\mathbf{k}}} \Theta_\chi(\mathbf{x}) d^3\mathbf{x}, \text{ where } V_{2\pi} = \int_{[0,2\pi]^3} \Theta_\chi(\mathbf{x}) d^3\mathbf{x} \tag{12}$$

The scaling of N_r, the number of boxes needed to cover the set, and of $\Sigma_{\mathbf{k}} \mu_\chi(B_{r,\mathbf{k}})^2$ is used to define the box-counting dimension and the box-counting-based correlation dimension, respectively. We thus compute

$$N_r = \sum_{\mathbf{k}} [\mu_\chi(B_{r,\mathbf{k}})]^0, \text{ where } \mu_\chi(B_{r,\mathbf{k}})^0 = \begin{cases} 1, & \text{if } \int_{B_{r,\mathbf{k}}} \Theta_\chi(\mathbf{x}) d^3\mathbf{x} > 0 \\ 0, & \text{otherwise} \end{cases} \tag{13}$$

as well as

$$\mathcal{M}_2(r) = \sum_{\mathbf{k}} [\mu_\chi(B_{r,\mathbf{k}})]^2 \tag{14}$$

The behaviour $N_r \sim (r/\eta)^{-D_0}$ defines the box-counting dimension D_0, and $\mathcal{M}_2(r) \sim (r/\eta)^{D_2}$ defines the box-counting-based correlation dimension, D_2 [14,40].

The implementation of the box-counting dimension is done as follows: the positions of all points in the set are histogrammed using the cubic-box boundaries as the bins boundaries. For each bin with non-zero count, the bin was normalised to 1, and all other bins are left to 0. The resulting histogram is summed, yielding the number of boxes that intersect the set of interest, N_r. The box size r ranges between 4.25 η and 850 η. For the box-counting-based correlation dimension, the computation is similar, but instead of normalising the resulting count, we compute the sum of the bin values squared, which amounts to the $\mu_\chi(B_{r,k})^2$ calculation.

The results for the box-counting dimension can be seen in Figure 3(a) and the box-counting-based correlation dimension plot is presented in Figure 3(b). The most notable

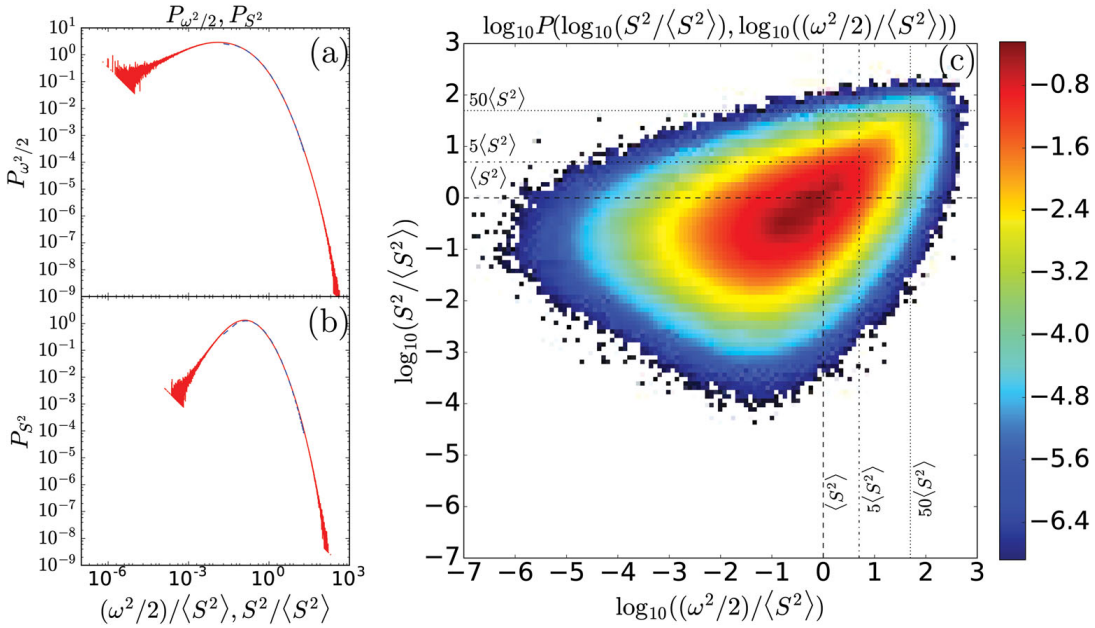

Figure 4. (a) Enstrophy and (b) Dissipation PDFs, computed from DNS of forced isotropic turbulence at $\mathrm{Re}_\lambda \sim 430$. The dashed blue line is the same PDF computed using a different analysis programme for this same data-set as reported in Ref. [41]. (c) Enstrophy and dissipation joint PDF. Similar PDFs can be found in Yeung et al. [42] for (a) and (b), and in Borue and Orszag [43] for (c).

feature of both plots is the lack of an inertial range scaling behaviour, in contrast with the structure function and the correlation dimension for the same set, Figure 2(a). One can discern a scaling at small scales $r < 20\,\eta$ approaching the integral scale. Similar conclusions are reached from the plots in Figure 3(b). Similar lack of scaling in the inertial range was reported by Moisy and Jiménez [23], for a lower Reynolds number DNS, which suggests that the lack of scaling may not be due to low Reynolds number only. Hence, no inertial-range power-law scaling is found for the box-counting approach applied to the excursion set of enstrophy. We have verified that the same is true for dissipation and all other variables considered in this paper (not shown but some limited results will be shown later). Hence, we focus our further analysis on the correlation-function-based analysis and scaling. We have tested that the correlation and box-counting algorithms yield correct results based on a 3D fractal set of known dimension (the Menger sponge), as summarised in Appendix 2.

3.3. Dependence on threshold, and dissipation-based excursion sets

In this section, we examine the correlation function scaling as a function of threshold and also present a similar analysis for the dissipation S^2. To place the thresholds in proper context, in Figure (4), we present the probability density function (PDF) for both enstrophy and dissipation, together with their joint PDF, for the data-set we used. Varying the threshold χ, we can probe different intensities of events, therefore different sectors of the PDFs. We present, in Figure (5), the results for the correlation functions for several thresholds, ranging from $\chi = 1\langle S^2\rangle$ to $\chi = 50\langle S^2\rangle$, for both enstrophy (see Figure 5(a,b))and for dissipation (Figure 5(c,d)).

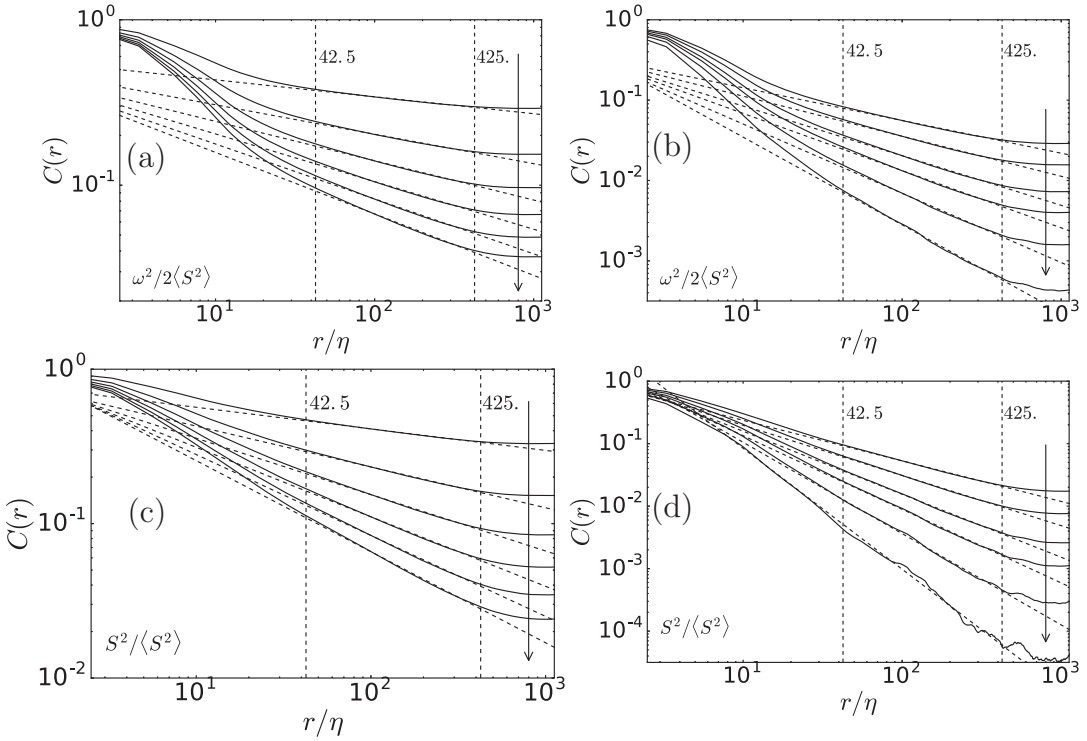

Figure 5. Radial correlation functions for enstrophy $\omega^2/2$ (a,b) and dissipation S^2 (c,d) computed from the DNS of forced isotropic turbulence at $\mathrm{Re}_\lambda \sim 430$. The thresholds χ range from $1\langle S^2\rangle$ to $50\langle S^2\rangle$. Thresholds are {1, 2, 3, 4, 5} for (a,c), and {7, 10, 15, 30, 50} for (b,d).

Clearly, all correlation functions shown in Figure 5 present power-law behaviour within the inertial range regardless of the observable probed and the value of the threshold. As expected, the correlation dimension has a monotonically decreasing behaviour as a function of the threshold, indicating that high-intensity sets become less and less space-filling. Such threshold dependence is not observed for a random non-intermittent field, as discussed in Appendix 3.

Comparing the values presented in Figure 5(a,c) with 5(b,d) confirms the initial observations made about Figure 1, in which is clear that the fractal dimensions associated with dissipation sets are systematically lower than the ones of the enstrophy sets, for the same thresholding value.

This behaviour is, initially, counterintuitive due to the expectation that enstrophy should be distributed along tubes, i.e. elongated 1D sets, while dissipation should be distributed along sheets. This behaviour is expected on the smallest, viscous, scales but does not seem to be reflected in the inertial range behaviour, at least not in the correlation function scaling.

Another feature visible in Figure 1 is that enstrophy and strain-rate are quite highly correlated, which can also be inferred from the overall shape of the joint PDF shown in Figure 4(c). Quantitatively, we confirmed this by computing the correlation coefficients as follows:

$$\rho(S^2, \omega^2/2) = \frac{\langle (S^2 - \langle S^2\rangle)(\omega^2/2 - \langle S^2\rangle)\rangle}{\langle (S^2 - \langle S^2\rangle)^2\rangle^{1/2}\langle (\omega^2/2 - \langle S^2\rangle)^2\rangle^{1/2}} = 0.61. \tag{15}$$

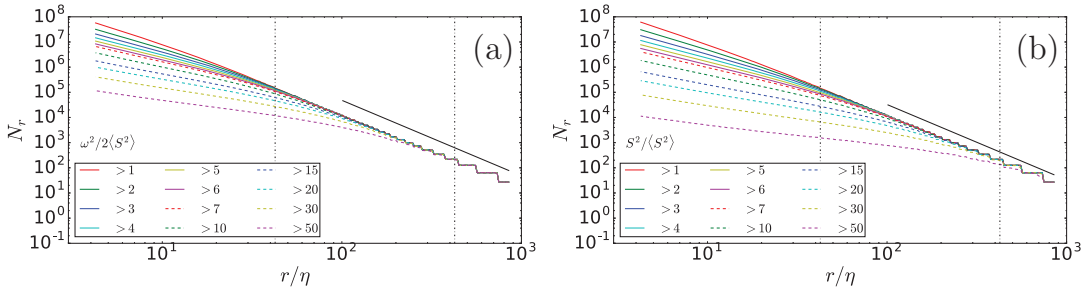

Figure 6. Box-counting dimension calculation for enstrophy (a) and dissipation (b) excursion sets showing lack of power-law scaling in the inertial range. The black line represents the $D_0 = 3$ scaling expected for large scales. The legend denotes $>\chi/\langle S^2\rangle$ threshold for each line.

$$\rho(\log S^2, \log \omega^2/2) = \frac{\langle(\log S^2/\langle S^2\rangle)(\log \omega^2/2\langle S^2\rangle)\rangle}{\langle(\log S^2/\langle S^2\rangle)^2\rangle^{1/2}\langle(\log \omega^2/2\langle S^2\rangle)^2\rangle^{1/2}} = 0.67. \tag{16}$$

The non-negligible correlation between enstrophy and dissipation has been noted before, see, e.g. [34–36].

For comparison, we present, in Figure 6, the box-counting dimension for these same sets, based on thresholding enstrophy and dissipation. They present the same features as in Figure 3(a,b). At the smallest scales, we can see that most high-enstrophy sets approach a slope of –1 but very high thresholds lead to even shallower (smaller-in-magnitude) slopes, consistent with broken-up, less coherent vortex events. For the dissipation structures, at small scales, we see a range of slopes between –2 for intermediate thresholds (consistent with sheets) but also decreasing continuously towards –1 and lower for higher thresholds. For larger scales, we notice again that all excursion sets saturate the box-counting to a slope of ~ -3 due to the homogeneity (space-fillingness) of the turbulence structures at the largest scales.

The lack of scaling of box-counting results in the inertial range make connection of the correlation function-based exponent $D(\chi) = 3 - \gamma_\chi$ with a fractal dimension not as clear as one would hope. Therefore, while from here on we will refer to $D(\chi) = 3 - \gamma_\chi$ as the correlation dimension, we must keep these limitations in mind.

4. Interval-based (iso) sets

An interesting alternative to considering the excursion sets is to compute interval-based sets, which correspond to the sets in which the observable is between χ_- and χ_+, a lower and an upper threshold, respectively. These sets are defined according to

$$\Theta^A_{\chi_+,\chi_-}(\mathbf{x}) = H(A(\mathbf{x}) - \chi_-)H(\chi_+ - A(\mathbf{x})) = \begin{cases} 1, & \text{if } \chi_- \le A(\mathbf{x}) \le \chi_+ \\ 0, & \text{otherwise} \end{cases} \tag{17}$$

They correspond to subsets of the excursion set near the lowest threshold, i.e. near the iso-threshold set bounding the excursion set. In fact, this procedure yields a good approximation for an 'iso-set' when $(\chi_+ - \chi_-)/\chi_- \ll 1$.

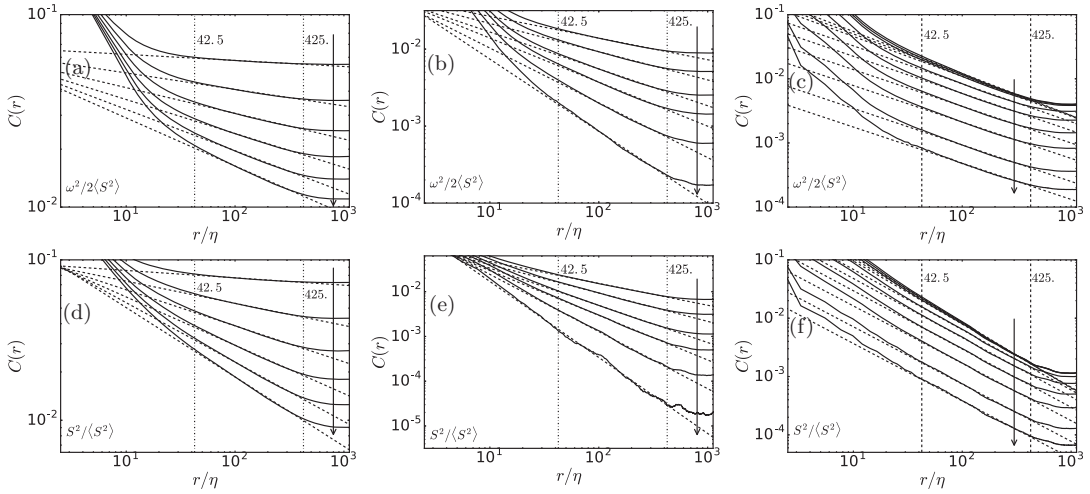

Figure 7. Radial correlation functions for enstrophy $\omega^2/2$ and dissipation S^2 computed from the DNS of forced isotropic turbulence at $\mathrm{Re}_\lambda \sim 430$. The thresholds χ range from $1\langle S^2\rangle$ to $50\langle S^2\rangle$. The results are for shells of thickness $\chi_+ - \chi_- = 0.05\chi_-$, for both enstrophy, (a) and (b), and for dissipation, (d) and (e). Thresholds are {1, 2, 3, 4, 5} for (a,d), and {7, 10, 15, 30, 50} for (b,e). As a band-width sensitivity test, we computed correlation functions for shells of varying thickness with base threshold $\chi_- = 20\langle S^2\rangle$, for both enstrophy (c) and dissipation (f), for thickness ranging from 100% to 0.5%. Legend denotes $\in [\chi_-/\langle S^2\rangle, \chi_+/\langle S^2\rangle]$ interval for each observable.

We compute the two-point correlation function using χ_- varying in the same set as the thresholds of the previous section, and $\chi_+ = 1.05\chi_- = (1 + \Delta)\chi_-$, which roughly corresponds to a thin shell of the inner boundary of the excursion set of threshold χ_-. We prefer a multiplicative, rather than additive, relationship between χ_+ and χ_- because it amounts to equally sized logarithmic bins. We also refer to these 'interval-based' sets as 'shell' sets.

The results of this analysis are presented in Figure 7(a,b) for enstrophy and in Figure 7(c,d) for dissipation. As is visible, the resulting two-point correlations also present robust power-law scaling in the same inertial range as the previous excursion set correlation functions.

In order to establish the robustness of results with regards to the 'thickness' of the band of thresholds defining the bin for the iso-set, we computed correlation functions for shells of varying thickness with base threshold $\chi_- = 20\langle S^2\rangle$, for both enstrophy and dissipation. As can be seen in Figure 7(c) for enstrophy, the resulting power-law can be observed to be robust regardless of the tested thickness. Also, the resulting exponent is insensitive to the thickness, unless very thick shells are used, in which case we are actually closer to an excursion set than to a proper interval-based (iso) set. A similar result can be obtained for the dissipation, as seen in Figure 7(f). Again, we repeated the box-counting dimensions computation for reference (not shown), and observed that there is no power-law in the inertial range.

To exemplify the difference in behaviour between excursion sets and interval-based sets correlation functions, we computed both types of sets for the lower threshold at $20\langle S^2\rangle$ in both cases. One observes that they differ, mostly, on the small r region, which is an imprint of the fact that shell-based sets have a 'hollow' shape compared to the excursion sets. The

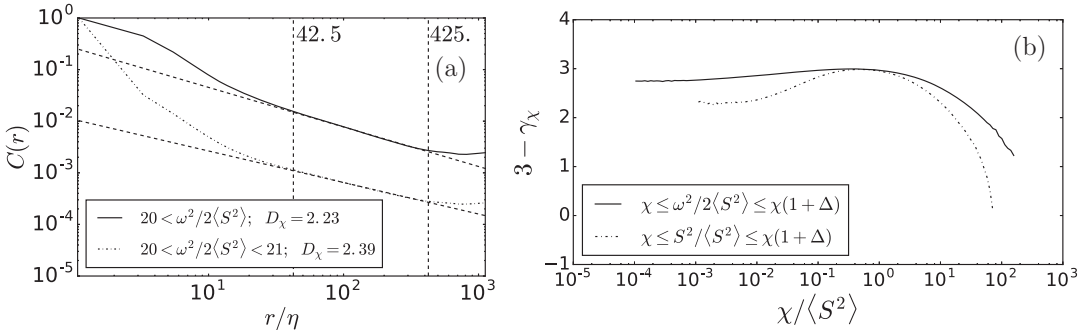

Figure 8. (a) Comparison of excursion sets with thin shell sets starting at similar threshold values; (b) Interval-based sets dimensions, as a function of the probed intensity $\chi/\langle S^2\rangle$.

absolute value of the normalised correlation function is lower for shells than for the respective excursion sets, due to lower volume fraction, as expected. The correlation slope is flatter, having a higher compensated exponent (i.e. more 'space-filling').

In order to present the complete information of scaling exponents as a function of threshold, we present $D(\chi) = 3 - \gamma_\chi$ as a function of threshold corresponding to logarithmically spaced bins. The computation is done for both enstrophy and dissipation shell sets. Overall, both observables present the same qualitative behaviour, but enstrophy consistently shows a higher correlation-based dimension. Prior results [30] have shown that enstrophy is 'more intermittent' than dissipation and thus the present results may appear to be counterintuitive, as mentioned before in section 3. Present results show that the decay of spatial correlation is slower with distance for the high enstrophy region as compared to the high dissipation regions which must be more 'broken-up' and less coherent, consistent with what is seen in the visualisation, Figure 1(b). We conjecture that the slow correlation decay reflects the underling highly elongated structure of high vorticity regions, which is not the same for most of the other observables.

The graph of dimension versus threshold in Figure 8(b) is reminiscent of the plots of singularity spectra $D(h)$ commonly measured via Legendre transforms in the multifractal formalism [11,12]. In order to establish a connection between the two approaches, we would need to know how to connect the local thresholds we use to the 'local singularity strength h'. It is expected that such a relationship will depend on Reynolds number and would also depend in non-trivial ways on prefactors. In the absence of a detailed analysis as function of Reynolds number, we cannot at this stage provide clear connection of the present results with the multifractal formalism and we relegate this aspect to future work.

5. Joint Iso-set analysis

As done for a single scalar, it is possible to define joint excursion sets for both enstrophy $\omega^2/2$ and dissipation $S^2 = S_{ij}S_{ij}$, according to

$$\begin{aligned}\Theta^{\omega\epsilon}_{\chi_\omega,\chi_\epsilon}(\mathbf{x}) &= \Theta(\omega^2/2 - \chi_\omega)\Theta(S^2 - \chi_\epsilon) \\ &= \begin{cases} 1, & \text{if } \omega^2 \ge \chi_\omega \text{ and } S^2 \ge \chi_\epsilon \\ 0, & \text{otherwise} \end{cases}\end{aligned} \tag{18}$$

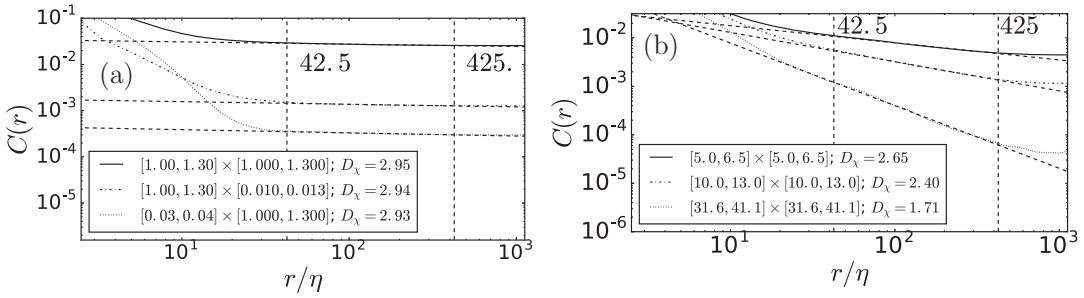

Figure 9. Set of representative log–log plots showing power-law scaling of the correlation functions for joint shell sets on enstrophy $\omega^2/2$ and dissipation S^2. Values correspond to ($\omega^2/2$, S^2) in the rectangle shown.

The radial correlation function of these sets are computed following the same approach as in the previous Section 3. Representative results are shown in Figure 9(a,b). We observe the same overall power-law behaviour seen in the single excursion sets, in the same range of length-scales corresponding to the inertial range. Similarly, we can define joint interval-based sets according to

$$\begin{aligned}\Theta^{\omega\epsilon}_{\chi_\omega,\chi_\epsilon,\Delta}(\mathbf{x}) &= \Theta(\omega^2/2-\chi_\omega)\Theta(\chi_\omega(1+\Delta_\omega)-\omega^2/2)\Theta(S^2-\chi_\epsilon)\Theta(\chi_\epsilon(1+\Delta_\epsilon)-S^2)\\ &= \begin{cases}1, & \text{if } \chi_\omega \le \omega^2/2 \le \chi_\omega(1+\Delta_\omega) \text{ and } \chi_\epsilon \le S^2 \le \chi_\epsilon(1+\Delta_\epsilon)\\ 0, & \text{otherwise}\end{cases}\end{aligned} \tag{19}$$

For very small spacings Δ, there might be numerical and statistical problems due to the very small number of points on a finite data-set. Therefore, the map of the joint two-point correlation function is only accurate for the centre-most region, away from the skirt of the joint probability distribution function, in Figure (10). Though not shown here, we also performed sensitivity analysis to the bin size, analogously to that presented in Figure 7(c,f), and similar results were obtained.

One feature we observe in Figure (10) is the presence of an inverted/rotated 'L-shaped' region of constant dimension, indicating a near independence of the geometrical distribution of one of the observables. This indicates that the regions with either average enstrophy or dissipation are dominated by space-filling geometry, irrespective of the value of the other quantity within those regions. As regions of very high or very low enstrophy and dissipation are probed, we observe lower and lower correlation dimension $D(\chi_\omega, \chi_\epsilon) = 3 - \gamma_{\chi_\omega,\chi_\epsilon}$, as expected. The lowest observed compensated exponent on the probed region is around $D(\chi_\omega, \chi_\epsilon) \approx 1.2$.

Considering the values along the diagonal where $S^2 = \omega^2/2$, or $Q = 0$, i.e. $D_{\text{diag}}(\chi) = D(\chi, \chi)$, we can approximate the joint distribution only in terms of this function, i.e. $D(\chi_\omega, \chi_\epsilon) \approx D_{\text{diag}}(\max\{\chi_\omega, \chi_\epsilon\})$. This approximation reproduces the L-shaped pattern quite well (not shown), suggesting that any $Q \neq 0$ regions have, to a first approximation, the dimension associated with the $Q = 0$ hull for the component with the highest intensity, of either S^2 or $\omega^2/2$.

Note that the shape of the joint distribution is remarkably similar to the contour plots of the conditional mean pressure reported in Yeung et al. [42]. While pressure depends

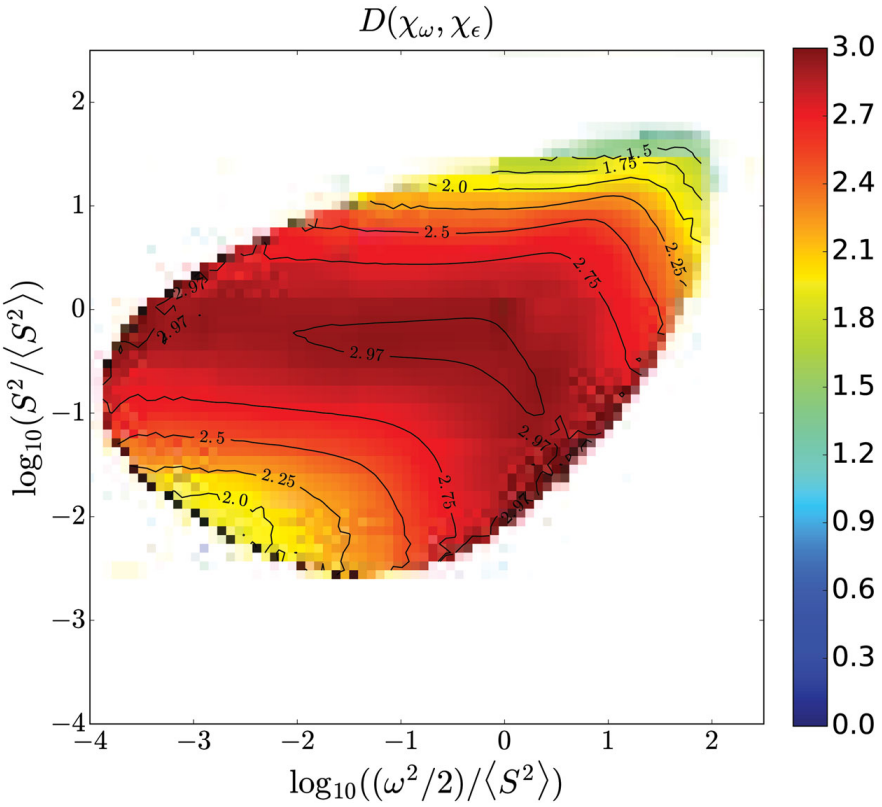

Figure 10. Joint correlation function exponent $D(\chi_\omega, \chi_\epsilon) = 3 - \gamma_{\chi_\omega,\chi_\epsilon}$ for joint interval-based sets, with equally spaced logarithmic bins $\Delta = \Delta_\omega = \Delta_\epsilon \approx 0.28$, with the same bins utilised to compute the joint PDF in Figure 4(c).

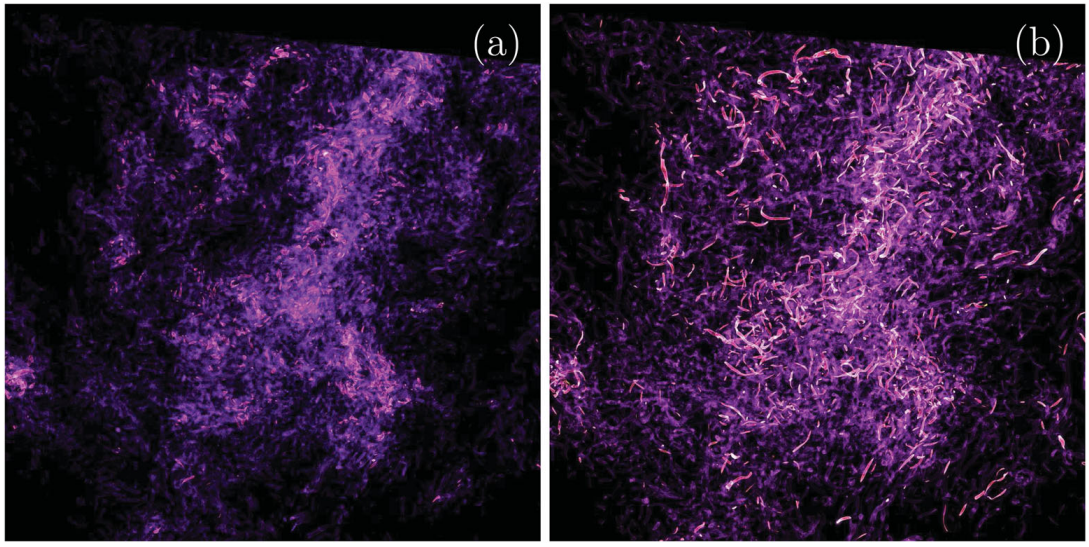

Figure 11. Volume rendering of (a) the Q velocity gradient invariant excursion set for negative $Q < -2\langle S^2\rangle$, i.e. corresponding to the function $Q_{\text{ex}}(\mathbf{x}) = -Q(\mathbf{x})\Theta^{-Q}_{2\langle S^2\rangle}(\mathbf{x})$ and (b) the Q excursion set for positive $Q > 2\langle S^2\rangle$, i.e. corresponding to the function $Q_{\text{ex}}(\mathbf{x}) = Q(\mathbf{x})\Theta^{Q}_{2\langle S^2\rangle}(\mathbf{x})$ on a 512^3 subset of the full data.

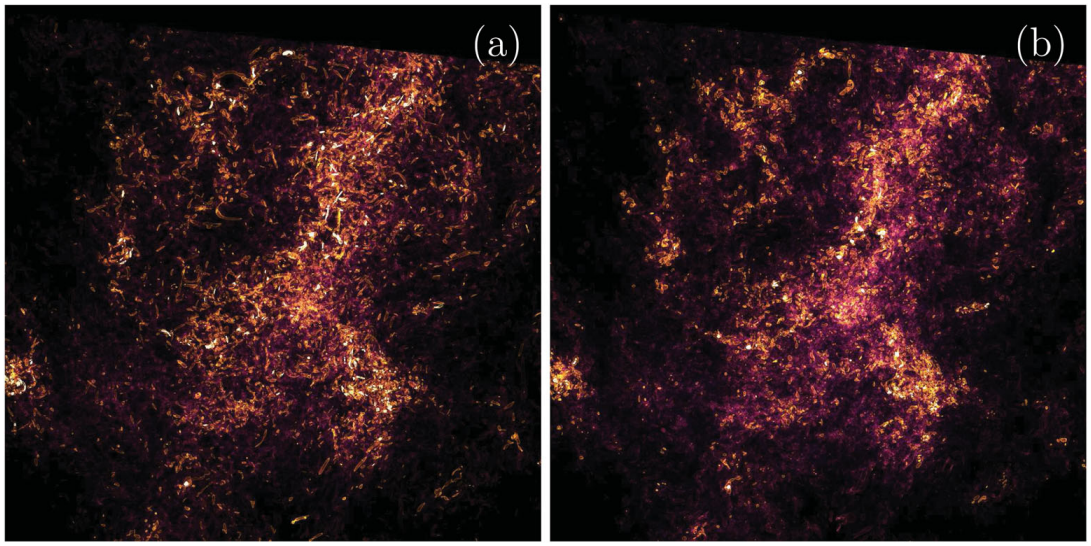

Figure 12. Volume rendering of (a) the R velocity gradient invariant excursion set corresponding to the function $R_{ex}(\mathbf{x}) = -R(\mathbf{x})\Theta^{-R}_{2\langle S^2\rangle}(\mathbf{x})$ and (b) of the R set corresponding to the function $R_{ex}(\mathbf{x}) = R(\mathbf{x})\Theta^{R}_{2\langle S^2\rangle}(\mathbf{x})$ on a subset of the full cube, with one-eighth in volume.

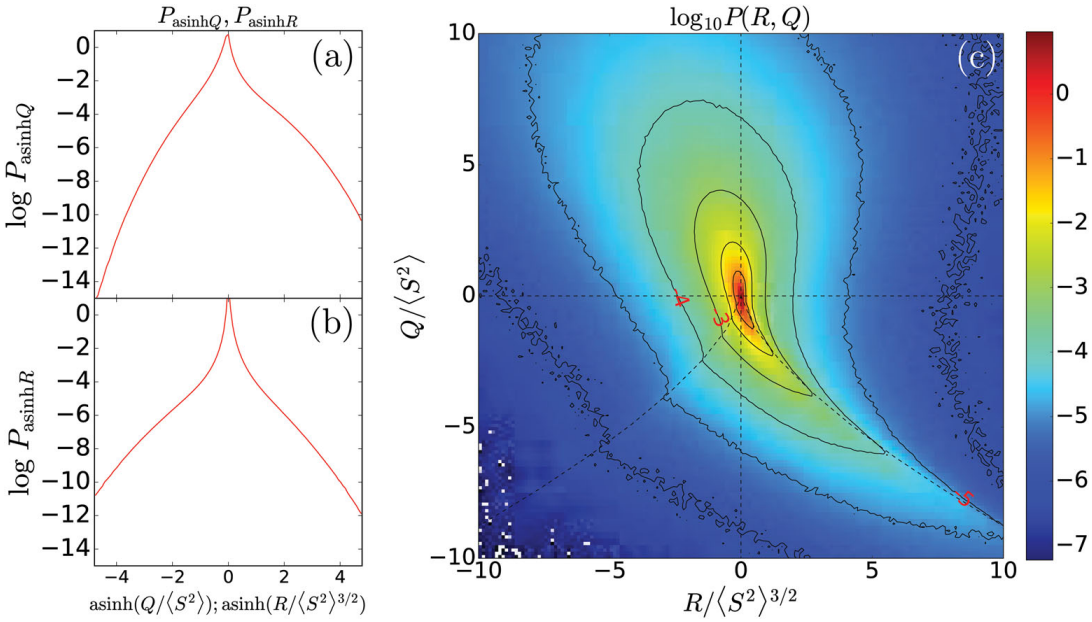

Figure 13. PDFs of Q (a) and R (b) PDFs. (c) Q and R joint PDF, a similar joint PDF can be seen in the reference Meneveau [45] and Nomura and Post [50].

directly on the spatial distribution of vorticity and strain-rate in the flow, establishing a direct connection to the correlation exponents appears non-trivial.

6. Scaling analysis of spatial distribution of invariants Q and R

Following the work done in the previous sections, we seek to probe the geometrical structure of the observables Q and R defined in Equation (4). Since both quantities are signed,

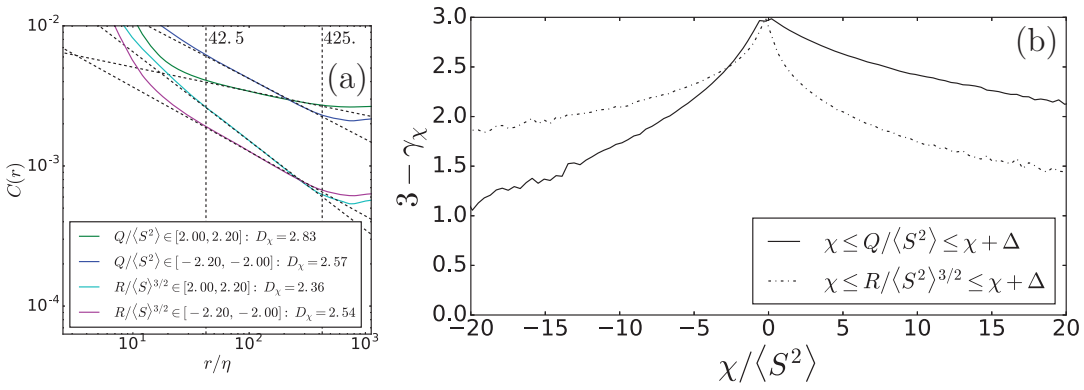

Figure 14. (a) Correlation functions for selected values of Q and R. (b) Correlation-based dimensions of joint interval-based sets, as a function of thresholds on Q and R .

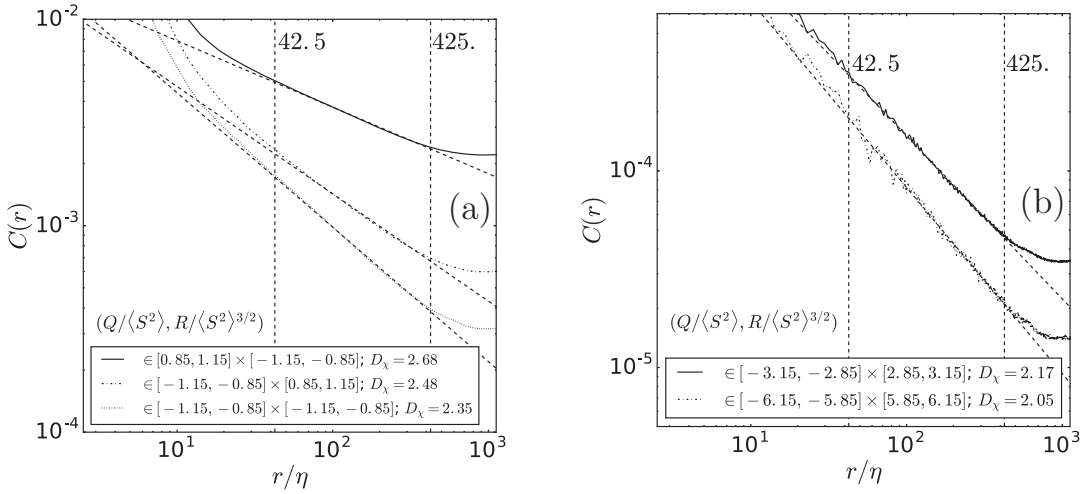

Figure 15. Set of representative log–log plots for power-law of the correlation functions for joint shell sets for Q and R velocity gradient invariants.

we computed their PDFs as function of thresholds in linear instead of logarithmic scale. First, we present the PDFs of both quantities, in Figure 13(a,b), and the joint PDF of Q and R in Figure 13(c). We notice the characteristic tear-drop shape in the joint PDF, with the right-most region following the so-called Vieillefosse tail as $Q = -\frac{3}{2^{3/2}}R^{2/3}$. More details can be found in Refs. [44–47].

The quantities in Figure 13(a,b) were plotted on inverse hyperbolic sine (asinh) axis. The asymptotic behaviour of asinh for large values is to approach log , while being linear close to the origin. These features allow us to have a reasonably undistorted view of the PDF near the origin, and also verify if there is any power-law behaviour on the tails of the PDF, for either positive or negative values of the quantities of interest. In this case, it appears that no power-law behaviour is visible in the tails of the PDFs of Q and R, on either positive or negative sides.

Before proceeding to analyse the spatial correlation functions of the corresponding shell sets, it is useful to present visualisations of the Q and R scalar fields. In Figure 11, we observe that the overall, middle and large-scale spatial distributions strongly resemble the

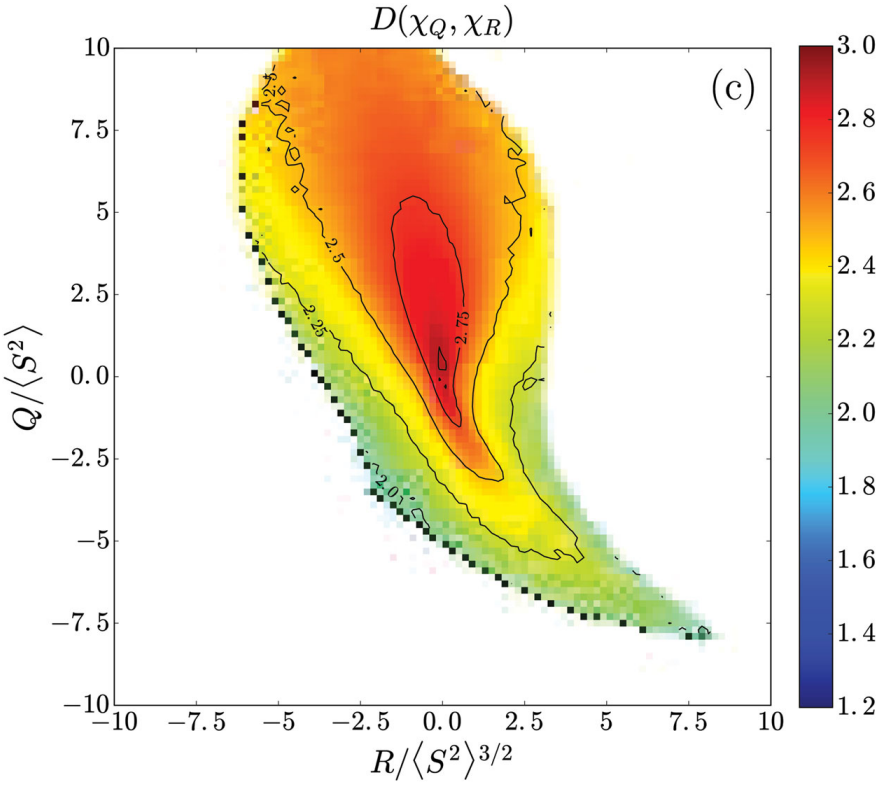

Figure 16. Joint correlation function exponent $D(\chi_\omega, \chi_\epsilon) = 3 - \gamma_{\chi_Q, \chi_R}$ for joint interval-based sets, with equally spaced linear bins $\Delta = \Delta_Q = \Delta_R = 0.2$.

ones present earlier in Figure 1, especially comparing Figure 1(a) and Figure 11(b). This resemblance is expected since $Q > 0$ thresholds are often used as vortex visualisations (the Q-criterion [48]). Negative Q regions are more correlated with high-straining region, again as expected based on the identity $Q = \omega^2/2 - S^2$.

Visualisations of spatial distributions of the scalar R are less common in the literature (although see discussion in Ref. [49]). Interestingly, we observe that negative R distributions, in Figure 12(a), include slightly more elongated structures than the positive R distributions, Figure 12(b). Hence, the regions in which both Q and R show elongated structures are in the upper-left quadrant of the RQ plane, the vortex-stretching quadrant.

To quantify the spatial correlation structure, the correlation functions of interval-sets are computed as before, for various thresholds of Q and R. Similar to what is observed for enstrophy and dissipation, we find clear power-laws in the two-point correlation functions associated with the iso-sets of Q and R, as exemplified in Figure 14(a).

The measured correlation dimensions, as a function of the threshold χ, are presented in Figure 14(b). The basic behaviour of the correlation dimension mimics the PDF of the corresponding observable, as can be seen comparing Figures 13(a,b) and 14(b).

For the analysis of joint Q and R sets, we present some representative log–log plots in Figure 15(a,b), which showcase that the correlation function presents power-law behaviour for these sets as well. The full joint correlation dimension distribution is presented in Figure 16.

The most striking feature of Figure (16) is the top–bottom asymmetry of the $Q > 0$ and $Q < 0$ regions for the correlation-based dimension. The dimension is clearly larger

in the rotation-dominated regions at $Q > 0$. This is consistent with the fact that, for the same threshold, correlation dimensions associated with enstrophy iso-sets are higher than dissipation iso-sets (Figure 8(b)). Clearly, the geometric features of the joint distribution differ from the joint PDF in Figure 13(c). That is to say, regions with high PDF need not have higher (more space-filling) correlation-based dimension.

7. Conclusions

We have analysed a turbulence data-set from DNS at a moderately high Reynolds number, with the specific aim to identify scaling laws characterising the spatial distribution of phenomena of various magnitudes. Both excursion sets and iso-sets (thin bands) have been considered for enstrophy, dissipation (or square-strain-rate) and the two invariants Q and R. The variable Q has also often been used for flow visualisation and high positive values of Q can be used to identify vortices. The spatial distributions are first defined using an indicator function and the radial correlation function of the indicator function distribution is evaluated. In all cases, we find clear power-law decay in these correlations for separation distances falling within the inertial range of turbulence. The scaling range is insensitive to the thresholds and variables of interest. We confirmed this is the same scaling range characterising power-law scaling of the traditional velocity structure function.

Even though the correlation functions present power-law in the inertial range, consistently with the results of Moisy and Jimenez [23], no such power-law behaviour is observed in box-counting and box-counting-based correlation dimension computations. Thus, the interpretation of the correlation-function-based exponents $D(\chi) = 3 - \gamma$ as a 'dimension' must be considered with care. Consistent with the definition of a dimension, for thresholds near the mean value, space-fillingness is observed with the exponent saturating at 3. For higher (or lower) thresholds, this correlation dimension reduces to lower values.

We also observe some surprising trends, such as a lower correlation-function-based dimension for strong dissipation events compared to strong enstrophy events. It is likely that this is caused by the elongated nature of vortices causing coherence in space over longer distances on average as compared to regions of high dissipation. We also show that sets defined by joint conditions on strain and enstrophy, and on Q and R, also display power-law scaling in the correlation functions, providing further characterisation of the complex spatial structure of the intersections of these sets.

The inertial range power-law behaviour of correlation functions associated with quantities in the viscous range (dissipation, enstrophy, Q and R) of a wide range of thresholds provides further evidence of geometric self-similarity of flow properties in the inertial range.

Overall, this work shows an alternate route to study the multifractal behaviour of turbulence, in which geometrical information is probed explicitly by using correlation functions of indicator functions. It is not yet immediately clear how to naturally connect the results of the present work with the traditional multi-fractal formalism, which is based on the scaling of statistical high-order moments of the box-averaged flow quantities over regions of different sizes. Specifically, it is not clear how to associate the threshold χ to the parameters α or h used in the multifractal formalism.

Further follow-up work should develop such correspondences, as well as examine the scaling for different (higher) Reynolds numbers. Also, extensions to non-isotropic shear flows, in which the correlation functions may decay differently in different directions, would be of interest.

Acknowledgements

The authors are grateful to the Turbulence Research Group members for discussions and help with this project, Dr Gerard Lemson and Dr Stephen Hamilton for their help with the SciServer system. José Hugo Elsas is grateful to the Rio de Janeiro state science funding agency FAPERJ program for international Ph.D. exchange, grant number E-26/200.076/2016 and to Dr L. Moriconi for authorising the international exchange. Alexander Szalay and Charles Meneveau are supported by NSF's CDS&E: CBET-1507469 and BigData:OCE-1633124 projects. The SciServer project is supported by NSF's DIBBS program (OAC-1261715). SciServer is a collaborative research environment for large-scale data-driven science. It is being developed at, and administered by, the Institute for Data Intensive Engineering and Science at Johns Hopkins University. SciServer is funded by the National Science Foundation Award ACI-1261715. For more information about SciServer, please visit http://www.sciserver.org.

Disclosure statement

No potential conflict of interest was reported by the authors.

Funding

Division of Chemical, Bioengineering, Environmental, and Transport Systems [grant number CBET-1507469]; Division of Ocean Sciences [grant number OCE-1633124]; Fundação Carlos Chagas Filho de Amparo à Pesquisa do Estado do Rio de Janeiro [grant number E-26/200.076/2016]; National Science Foundation [grant number OAC-1261715]; Office of Cyberinfrastructure [grant number ACI-1261715, [grant number OAC- 1261715].

References

[1] Frisch U. Turbulence. The legacy of A. N. Kolmogorov. Cambridge (UK): Cambridge University Press; 1995. ISBN 0-521-45103-5.
[2] Kolmogorov AN. The local structure of turbulence in incompressible viscous fluid for very large Reynolds numbers. Proc USSR Academy Sci. 1941;30:299–303.
[3] Kolmogorov AN. A refinement of previous hypotheses concerning the local structure of turbulence in a viscous incompressible fluid at high Reynolds number. J Fluid Mech. 1962;13(1:82–85. DOI: 10.1017/S0022112062000518.
[4] Obukhov AM. Some specific features of atmospheric turbulence. J Fluid Mech. 1962;13(1:77–81. DOI: 10.1017/S0022112062000506.
[5] Novikov EA, Stewart RW. Intermittency of turbulence and the spectrum of fluctuations of energy dissipation. Izv Akad Nauk SSSR Geofiz. 1964;3:408.
[6] Novikov EA. Scale similarity for random fields. Soviet Phys Doklady. 1969;14:104.
[7] Novikov EA. Intermittency and scale similarity in the structure of a turbulent flow. Prikl Mat Mech. 1971;35:266–277.
[8] Novikov EA. The effects of intermittency on statistical characteristics of turbulence and scale similarity of breakdown coefficients. Phys Fluids Fluid Dyn. 1990;2(5):814–820. DOI: 10.1063/1.857629. Available from: http://dx.doi.org/10.1063/1.857629.
[9] Mandelbrot BB. Intermittent turbulence in self-similar cascades: divergence of high moments and dimension of the carrier. J Fluid Mech. 1974;62(2:331–358. DOI: 10.1017/S0022112074000711.
[10] Frisch U, Sulem PL, Nelkin M. A simple dynamical model of intermittent fully developed turbulence. J Fluid Mech. 1978;87(4:719–736. DOI: 10.1017/S0022112078001846.
[11] Frisch U, Parisi G. On the singularity structure of fully developed turbulence. In: Turbulence and predictability in geophysical fluid dynamics and climate dynamics. Varenna (Italy),

Amsterdam (NY), North-Holland. (Proceedings of the International School of Physics Enrico Fermi series); 1985. p. 84–87.
[12] Benzi R, Paladin G, Parisi G, et al. On the multifractal nature of fully developed turbulence and chaotic systems. J Phys Math Gen. 1984;17(18):3521. Available from: http://stacks.iop.org/0305-4470/17/i=18/a=021.
[13] Meneveau C, Sreenivasan KR. Simple multifractal cascade model for fully developed turbulence. Phys Rev Lett. 1987;59:1424–1427.
[14] Meneveau C, Sreenivasan KR. The multifractal nature of turbulent energy dissipation. J Fluid Mech. 1991;224:429–484.
[15] Sreenivasan KR. Fractals and multifractals in fluid turbulence. Ann Rev Fluid Mech. 1991;23(1):539–604.
[16] Ishihara T, Gotoh T, Kaneda Y. Study of high-Reynolds number isotropic turbulence by direct numerical simulation. Ann Rev Fluid Mech. 2009;41:165–180.
[17] Ishihara T, Higuchi H. Multifractal analysis by using high-resolution direct numerical simulation of turbulence. Dordrecht: Springer; 2008. p. 61–66.
[18] Meneveau C, O'Neil J. Scaling laws of the dissipation rate of turbulent subgrid-scale kinetic energy. Phys Rev E. 1994;49:2866–2874.
[19] Biferale L, Calzavarini E, Toschi F. Multi-time multi-scale correlation functions in hydrodynamic turbulence. Phys Fluids. 2011;23(8):085107. DOI: 10.1063/1.3623466.
[20] Benzi R, Ciliberto S, Tripiccione R, et al. Extended self-similarity in turbulent flows. Phys Rev E. 1993;48:R29–R32. DOI: 10.1103/PhysRevE.48.R29. Available from: https://link.aps.org/doi/10.1103/PhysRevE.48.R29.
[21] Meneveau C. Transition between viscous and inertial-range scaling of turbulence structure functions. Phys Rev E. 1996;54:3657–3663.
[22] Meneveau C, Sreenivasan KR. Measurement of $f(\alpha)$ from scaling of histograms, and applications to dynamical systems and fully developed turbulence. Phys Lett A. 1989;137(3):103–112.
[23] Moisy F, Jiménez J. Geometry and clustering of intense structures in isotropic turbulence. J Fluid Mech. 2004;513:111–133.
[24] Adler RJ. The geometry of random fields. Philadelphia (PA): SIAM; 2010.
[25] Novikov D, Feldman HA, Shandarin SF. Minkowski functionals and cluster analysis for CMB maps. Int J Modern Phys D. 1999;8(03):291–306.
[26] Mecke KR, Buchert T, Wagner H. Robust morphological measures for large scale structure in the universe. Astron Astrophys. 1994;288:697–704.
[27] Calvo MAA, Shandarin SF, Szalay A. Geometry of the cosmic web: Minkowski functionals from the Delaunay tessellation. In: 2010 International Symposium on Voronoi Diagrams in Science and Engineering (ISVD) 2010 Jun 28–30; Quebec (QC): IEEE; 2010. p. 235–243.
[28] Vincent A, Meneguzzi M. The spatial structure and statistical properties of homogeneous turbulence. J Fluid Mech. 1991;225:1–20.
[29] Jiménez J, Wray AA, Saffman PG, et al. The structure of intense vorticity in isotropic turbulence. J Fluid Mech. 1993;255:65–90. DOI: 10.1017/S0022112093002393.
[30] Meneveau C, Sreenivasan KR, Kailasnath P, et al. Joint multifractal measures: theory and applications to turbulence. Phys Rev A. 1990;41:894–913.
[31] Meneveau C. Lagrangian dynamics and models of the velocity gradient tensor in turbulent flows. Ann Rev Fluid Mech. 2011a;43:219–245.
[32] Li Y, Perlman E, Wan M, et al. A public turbulence database cluster and applications to study Lagrangian evolution of velocity increments in turbulence. J Turbul. 2008;9:N31.
[33] Bershadskii A, Kit E, Tsinober A, et al. Strongly localized events of energy, dissipation, enstrophy and enstrophy generation in turbulent flows. Fluid Dyn Res. 1994;14(2):71–101. ISSN 0169-5983.
[34] Zhu Y, Antonia RA. On the correlation between enstrophy and energy dissipation rate in a turbulent wake. Appl Sci Res. 1996;57(3):337–347.
[35] Donzis DA, Yeung PK, Sreenivasan KR. Dissipation and enstrophy in isotropic turbulence: resolution effects and scaling in direct numerical simulations. Phys Fluids. 2008;20(4):045108. DOI: 10.1063/1.2907227.

[36] Guala M, Liberzon A, Tsinober A, et al. An experimental investigation on Lagrangian correlations of small-scale turbulence at low Reynolds number. J Fluid Mech. 2007;574:405–427. DOI: 10.1017/S0022112006004204.
[37] Mandelbrot BB. The fractal geometry of nature. New York (NY): Henry Holt and Company; 1982. ISBN 9780716711865. Available from: https://books.google.com/books?id=0R2LkE3N7-oC.
[38] Johnson PL, Meneveau C. A closure for Lagrangian velocity gradient evolution in turbulence using recent-deformation mapping of initially Gaussian fields. J Fluid Mech. 2016;804:387–419. DOI: 10.1017/jfm.2016.551.
[39] Turk MJ, Smith BD, Oishi JS, et al. Yt: a multi-code analysis toolkit for astrophysical simulation data. Astrophys J Suppl Ser. 2011;192:9.
[40] Hentschel HGE, Procaccia I. The infinite number of generalized dimensions of fractals and strange attractors. Phys Non Phenom. 1983;8(3):435–444.
[41] Johnson PL, Meneveau C. Large-deviation joint statistics of the finite-time Lyapunov spectrum in isotropic turbulence. Phys Fluids. 2015;27(8):085110.
[42] Yeung PK, Donzis DA, Sreenivasan KR. Dissipation, enstrophy and pressure statistics in turbulence simulations at high Reynolds numbers. J Fluid Mech. 2012;700:5–15. DOI: 10.1017/jfm.2012.5.
[43] Borue V, Orszag SA. Local energy flux and subgrid-scale statistics in three-dimensional turbulence. J Fluid Mech. 1998;366:1–31.
[44] Vieillefosse P. Local interaction between vorticity and shear in a perfect incompressible fluid. J de Phys. 1982;43(6):837–842.
[45] Meneveau C. Lagrangian dynamics and models of the velocity gradient tensor in turbulent flows. Ann Rev Fluid Mech. 2011b;43:219–245.
[46] Naso A, Pumir A, Chertkov M. Statistical geometry in homogeneous and isotropic turbulence. J Turbul. 2007;8:N39. DOI: 10.1080/14685240701615978.
[47] Martín J, Ooi A, Chong MS, et al. Dynamics of the velocity gradient tensor invariants in isotropic turbulence. Phys Fluids. 1998;10(9):2336–2346.
[48] Hunt JCR, Wray AA, Moin P. Eddies, streams, and convergence zones in turbulent flows. Proceedings of Summer Program. Stanford (CA): CTR; 1988.
[49] Chong MS, Perry AE, Cantwell BJ. A general classification of three-dimensional flow fields. Phys Fluids. 1990;2:765–777.
[50] Nomura KK, Post GK. The structure and dynamics of vorticity and rate of strain in incompressible homogeneous turbulence. J Fluid Mech. 1998;377:65–97. DOI: 10.1017/S0022112098003024.

Appendices

Appendix 1. analysis environment on SciServer, and notebooks

The data used in this paper is obtained from the Johns Hopkins Turbulence Database (JHTDB). Most prior uses of JHTDB focused on the analysis of spatially localised regions, for which local operations such as interpolation or finite-difference-based differentiations could be done on the database system itself and deliver small amounts of data to users. In the present work, we desired instead to use FFTs for the analysis in order to enable us spectral accuracy for derivative evaluations, as well as efficient evaluation of the 3D correlation functions. However, FFTs require access to the entire 1024^3 fields, for which the usual access modes of JHTDB are not well suited. Instead, the analysis presented in this paper was performed on the Sciserver cloud environment, hosted by the Institute for Data Intensive Science at Johns Hopkins University (http://www.sciserver.org). The goal of Sciserver is to provide a local environment for data-driven science. Some screen shots can be seen

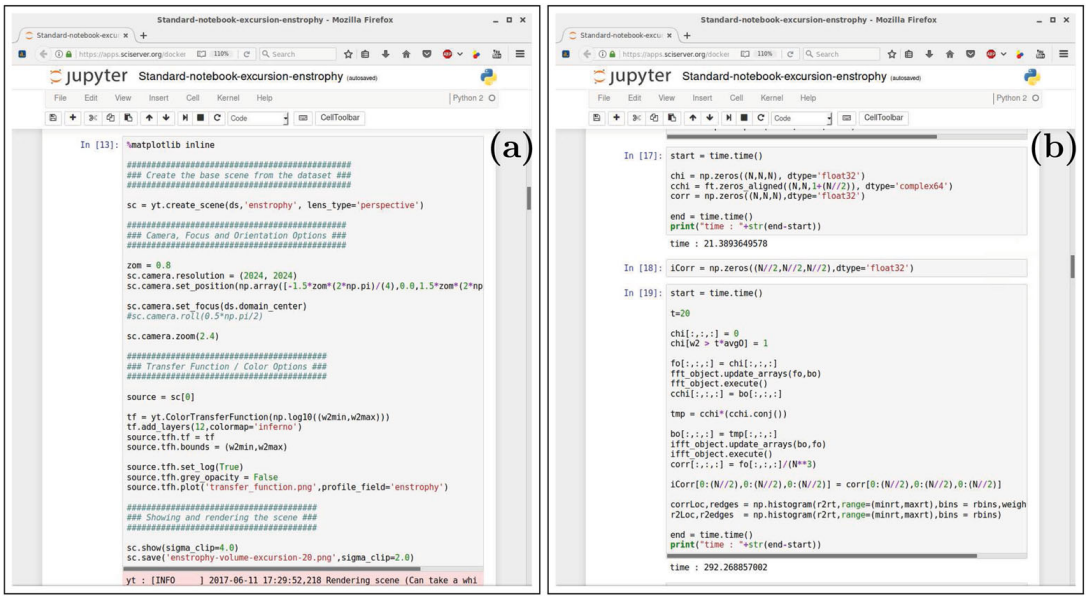

Figure A1. Code snippets used in the Sciserver environment: (a) Volume-rendering script with YT library; (b) Two-point correlation function.

in Figure A1. Sciserver provides a 10 Gigabit ethernet connection to the JHTDB [32,38], which is a valuable asset to the present work since it allows to easily download entire snapshots from the database. Sciserver was initially developed to be used in conjunction with the Sloan Digital Sky Survey, in the form of Skyserver, as a nearline analysis tool to the Astronomy database. It has since then expanded to other areas of scientific research including turbulence, genomics and oceanography.

We utilised the Compute module of Sciserver, which provides a Jupyter notebook environment running over Docker containers that provide user package customisability through Anaconda and Pip package managers. Sciserver also provides a set of pre-configured docker containers for Python, Matlab and other languages.

The notebook runs on a docker container with access to 24 CPU cores and 256 Gigabytes of random access memory (RAM). The docker container runs on top of a virtual machine (VM), which is shared among many containers.

Most of the analysis was done running Python code on the Jupyter notebooks, which allow us to integrate data analysis and documentation. Some of the most compute-intensive figures were produced on Python running on batch mode instead of inside the notebook, more specifically Figures (10) and (16)c, which correspond to the fractal dimension for the iso-sets for, respectively, joint enstrophy and strain-rate, and joint Q and R. These calculations required the evaluation of forward and inverse 3D FFTs for each of the 120×120 geometric sets, i.e. a significant computational effort. To perform the 3D FFTs efficiently, a data-cube must fit in the RAM of a single compute node.

The present analysis mode shows that, under appropriate circumstances, using Python on Jupyter notebooks within Sciserver is a viable option to perform global analysis of large DNS data-sets that have been stored in a database such as JHTDB.

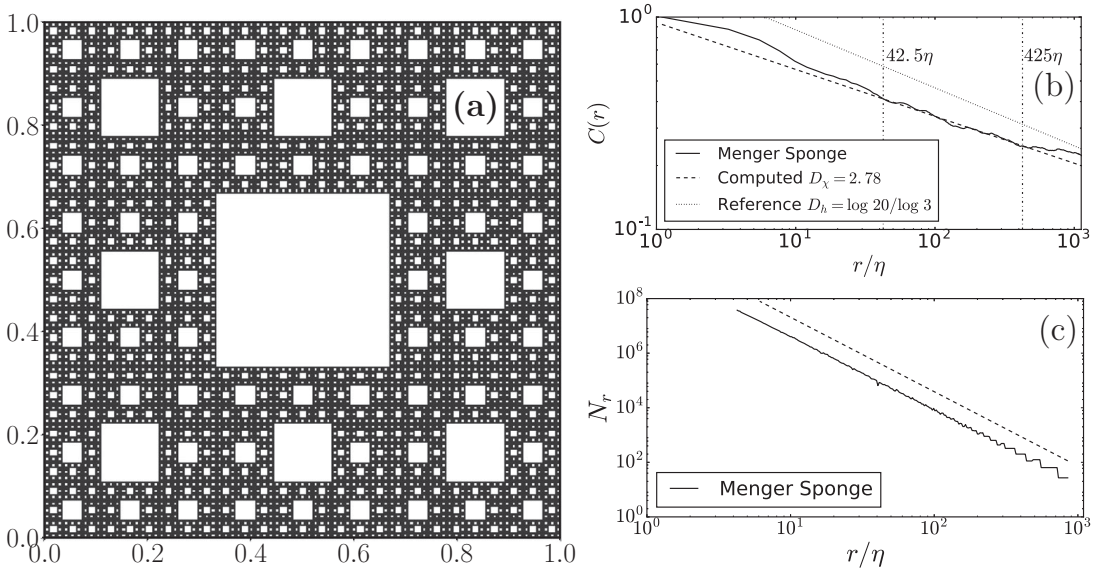

Figure B1. (a) Contour plot of a planar cut through an indicator function marking a 5-level Menger Sponge set; (b) Two-point radial correlation function for the Menger Sponge set; (c) Box-counting plot. The dotted line is the slope corresponding to the analytically known fractal dimension of the Menger Sponge ($D_0 = D_2 = \log(20)/\log(3)$).

Appendix 2. tests of correlation and box-counting on known fractal sets in 3D: Menger Sponge

In order to validate our techniques and present a known reference for the scaling tools utilised in this work, we present here the results of the correlation-function and box-counting-based analysis for a known self-similar fractal (the Menger Sponge).

The Menger Sponge is generated through an iterative process, in which the central one-third-sized sub-cube on each of the six sides and the core of the mother cube are deleted. This process is repeated iteratively for each remaining sub-cube. In our tests, we use a level 5 Menger sponge, i.e. the fifth iteration of removal as shown in Figure B1(a). The set indicator function is computed over the same $N^3 = 1024^3$ used for the data-set of this work, in which the removed regions are set to 0, and the rest is set to 1 (on elements of scale $1024/3^5 \sim 4$).

Over this indicator function, we compute the two-point correlation function just as in Section 2, which results in Figure B1(b). The power-law behaviour is affected at large and small scales due to the cubic symmetry of the set being analysed via spherical bins of distances. Still, there is clearly a power-law in a central decade in Figure B1(b) with a slope consistent with a correlation-function-based dimension of $3 - \gamma = \log 20/\log 3$, the Haussdorff dimension of the Menger sponge. Analogously, we computed the box-counting graph for the same indicator function. Since the box-counting method is consistent with the artificial fractal set's construction, one obtains a clearer power-law, as seen in Figure B1(c). Again, the slope is consistent with the Haussdorff dimension. These tests verify our method of computing the correlation function and box-counting-based scaling exponents.

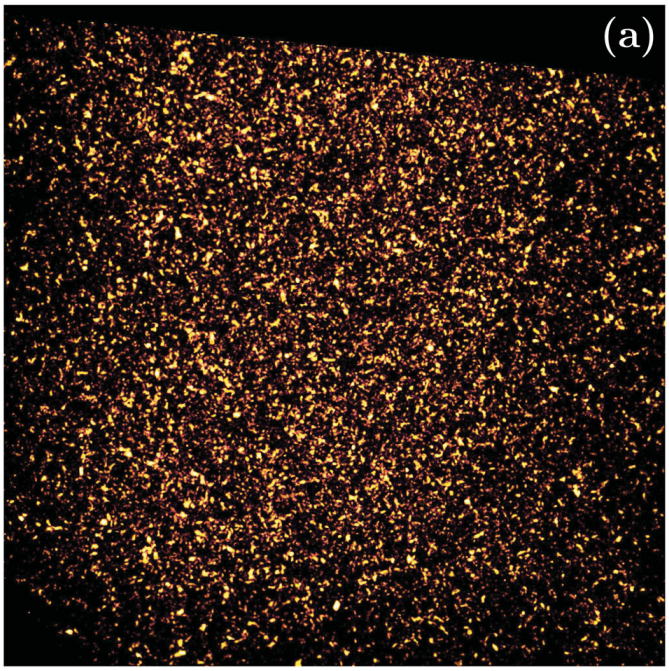

Figure C1. Visualisation of the non-intermittent enstrophy field excursion set for threshold $t = 5\langle S^2 \rangle$.

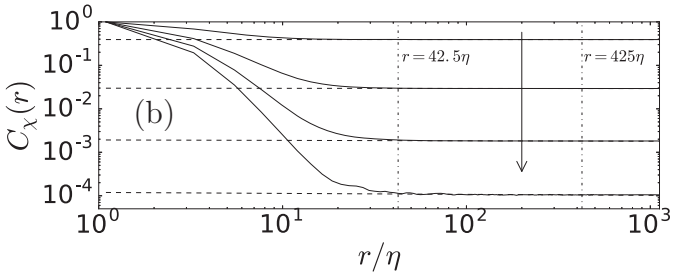

Figure C2. Two-point correlation function for excursion sets of enstrophy for thresholds $t = \{1, 3, 5, 7\}$.

Appendix 3. tests of correlation for random K41 field

In order to elucidate the connection of threshold dependence of the two-point correlation functions with the multifractality of the turbulent field, we perform the same analysis for a non-intermittent field with the same spectrum as the original field.

The resulting field can be visualised in Figure C1, which can be seen to have near to no structure besides small-scale clumping. This field has, accordingly, suppressed high-intensity events. The direct consequence is that the two-point correlation function produces a space-filling $\gamma_\chi = 0$ result, as seen in Figure C2 regardless of the threshold used, in this case for excursion sets on enstrophy. The same result can be found for iso-sets and also for other observables.

The random field is obtained by randomising the phases of the original velocity field, removing the divergence-full part of the resulting field and then correcting the spectrum to be the same as the original velocity field. This produces a divergence-free non-intermittent field, which is expected to also be statistically isotropic and homogeneous, which is confirmed by the results obtained.